PERGAMON

International Journal of Heat and Mass Transfer 41 (1998) 3299–3308

International Journal of HEAT and MASS TRANSFER

Beam focusing characteristics effect on energy reflection and absorption in a drilling or welding cavity of paraboloid of revolution

P. S. Wei*[a], C. Y. Ho[b]

[a] *Institute of Mechanical Engineering, National Sun Yat-Sen University, Kaohsiung, Taiwan, China*
[b] *Hura Hsia College of Technology and Commerce, Taipei, Taiwan, China*

Received 5 August 1996; in final form 10 November 1997

Abstract

Energy flux absorbed by the cavity of a paraboloid of revolution subject to a focused high-intensity beam, is systematically and quantitatively investigated. The intensity of incident flux is a Gaussian distribution, which is specified by the convergence angle, energy distribution parameter at the focal spot, and focal spot location relative to the workpiece surface. Absorption and scattering within the plasma in the cavity is assumed to be negligible. Using both analytical and Monte Carlo methods, and accounting for specular and diffuse reflections, the results find that energies absorbed by the cavity exhibit distinct regions for the focal spot lying above the cavity base. On the other hand, if the focal spot is below the base, absorbed energy flux is similar to a Gaussian distribution, and the maximum absorption is achieved. The effects of the beam focusing characteristics on the distribution of absorbed flux are provided. Formations of weld defects such as spiking and abnormally expanded fusion zone are proposed.

Nomenclature

A area
A_n beam cross-section
F view factor
f focal spot location $= \hat{f}/r_0$, as shown in Fig. 1
f_n fraction, as found from equations (12) and (15)
F_{ij} transfer factor, as defined in equation (4)
h cavity depth $= \hat{h}/r_0$, as shown in Fig. 1.
P fraction function, as presented in equations (5) and (6)
q incident flux $= \hat{q}r_0^2/Q$
Q beam power
q_w dimensionless energy flux absorbed by cavity wall
r radial coordinate $= \hat{r}/r_0$
r_f focal spot size $= \hat{r}_f/r_0$, as shown in Fig. 1
$\mathbf{R}_{ij}$ vector of energy bundle from point i to j
$\mathbf{R}'_{ij}$ vector of specularly reflected ray at point j
r_S critical or minimum radius of region II, $r_S = \hat{r}_s/r_0$
r'_s location of the first striking point of energy ray whose second specularly striking point is $r_3 = 1$
r_0 dimensional cavity opening radius, as shown in Fig. 1
s distance, defined in equation (3)
s_0 $r_f/\tan\beta + \text{sign}(f+h)(f+h)$, as shown in Fig. 1
W diffuse radiosity.

Greek symbols

α absorptivity
β half convergence angle
β' incident angle of an energy ray, as shown in Fig. 1
ε emissivity
θ cone angle measured from normal line
ρ_d, ρ_s diffuse and specular reflectivity
ϕ circumferential angle on x–y plane
ψ inclination angle of cavity wall, as shown in Fig. 1.

Superscript

$\hat{}$ dimensional quantity

* Corresponding author.

0017–9310/98 $19.00
PII: S0017–9310(98)00036–2

Subscripts

i, j starting and receiving point
jn first striking point of *n* times specular reflection
n normal to cavity or number of contacts
0 point source or cavity opening
r reflection.

1. Introduction

Welding, drilling, and cutting with a focused high-intensity beam (laser, electron beam, or plasma arc) are characterized by a deep and narrow vapor-filled cavity. In order to understand these processes, two important factors, which are the beam focusing characteristics and reflections of the beam by the cavity wall, should be taken into account. This becomes the objective of the present work.

Adams [1, 2] observed that the maximum joint penetration was achieved with the beam focused about 2.54 cm below the surface of a stainless steel in low- and high-voltage electron-beam welding. The effects of the focusing characteristics specified by the size, convergence angle, and location of the focal spot on high-power-density-beam welding are theoretically investigated by Wei and Chow [3].

The abnormally expanded fusion zone, however, was not obtained. This defect may result from specular reflections of the incident flux. The significant effect of reflections on drilling was experimentally examined by Arata [4]. In view of reflections by cavity walls, an increase in the gap between workpieces resulted in the opening diameter of the cavity in the bottom workpiece to be larger than the cavity diameter at the bottom surface of the top workpiece.

Absorbed energy by the cavity by accounting for reflections is quite different from the incident flux. Using a Monte Carlo method [5], Wang and Wei [6] found that energy absorbed by the cavity of a paraboloid of revolution subject to a collimated parallel beam of Gaussian and uniform distributions exhibits distinct regions determined by a dimensionless critical radius r_S. In the central region where radii $r < r_S$, the wall is irradiated by a direct incident energy-beam; while for $r \geqslant r_S$, the wall experiences the first specularly reflected energy from itself in addition to the direct incident energy. A jump which can be a hundred time of the incident flux may occur near the critical radius.

The focusing characteristics are closely related to weld defects. Konkol et al. [7] observed that as the focal spot of an electron-beam was lowered from above to below the workpiece surface vertical cross-sections were changed from convex to parallel-sided to V-shaped. Spiking representing non-uniform in depth was pronounced at the bottom of V-shaped fusion zones. Intensity of the incident flux was a cause of spiking, as investigated by Armstrong [8] and Giedt [9]. The focal location is also responsible for shrinkage cavities and the abnormally expanded fusion zone at the middle portion of deep penetration, as proposed and observed by Schiller et al. [10] and Irie et al. [11], respectively.

The present work investigates a cavity of paraboloid of revolution irradiated by a focused incident flux of Gaussian distributions. Not only the beam focusing characteristics, but also specular and diffuse reflections by the wall, are accounted for. A more relevant energy transport to the workpieces is therefore determined.

2. System model

As illustrated in Fig. 1, a focused incident flux on a cavity of paraboloid of revolution can be partially absorbed and the remainder specularly and diffusely reflected. The focal spot from the workpiece surface is denoted by f being positive above the surface and negative below the surface. The spot size and convergence angle of the beam are r_f and 2β, respectively. Incident flux with the focal spot above the cavity base can be considered as emitted by a virtual point source S, as illustrated in Fig. 2(a). When the focal spot lies below the cavity base, energy is emitted by an imaged point source S', as shown in Fig. 2(b). The primary assumptions are made as follows

(1) The incident flux is a Gaussian distribution at any transverse cross-section [12]. As for a laser-beam,

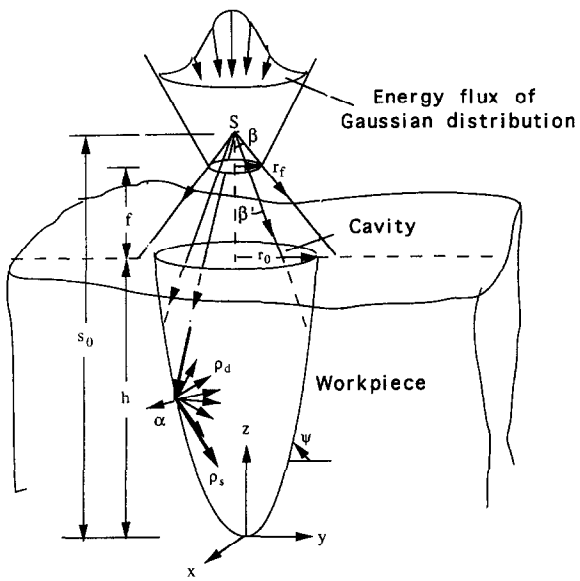

Fig. 1. Physical model indicating energy absorbed and reflected specularly and diffusely in the cavity of paraboloid of revolution produced by a focused beam.

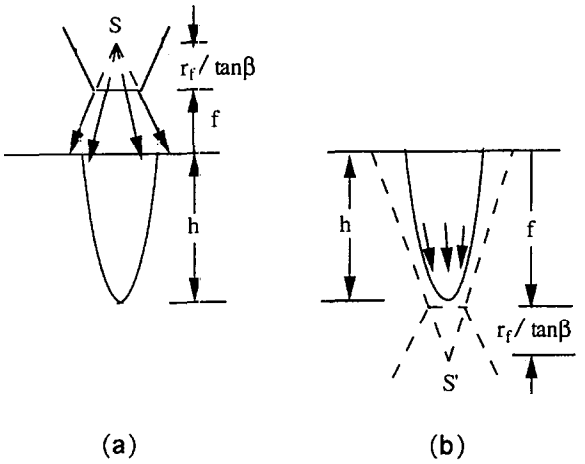

Fig. 2. Energy emitted by (a) a virtual point source at S, and (b) an imaged point source at S'.

the Gaussian distribution is valid for the spatially coherent TEM_{00} model.

(2) The cavity is idealized by a paraboloid of revolution to a first approximation [13].

(3) The cavity is stationary, even though drilling or welding is unsteady. This is because the time scale for energy redistribution can be estimated to be around 10^{-10} s, which is much smaller than 10^{-3} s for drilling a cavity, as measured by Miyazaki [14].

(4) The cavity is a specular and diffuse reflector; so as to simplify the problem without loss of generality, the surface is modeled by choosing appropriate values of specular and diffuse reflectivities. Then the radiative properties are independent of direction and wavelength of the energy-beam.

(5) Absorption within the plasma in the cavity is ignored. Temperatures and concentrations of electrons in iron plasmas during deep welding with a continuous CO_2 laser were measured by Poueyo-Verwaerde et al. [15] and Collur and DebRoy [16] to be as high as 7000 K and 9×10^{23} particles/m^3, respectively. The absorption length due to electron-neutral interactions therefore is 0.25 m, while that resulting from electron-ionized iron is 0.03 m. As a consequence, 80% ± 10% of a beam power of 15 kW, and 92% ± 5% of 1 kW are transmitted.

(6) Radiation in the plasma is neglected. Emission due to free-bound transitions, which are dominant in plasmas, was less than 5×10^8 W/m^2 for temperatures below 10 000 K and vapor densities around 10^{25} particles/m^3 [17]. Radiation from the plasma thus is only 1% of the incident flux.

(7) Scattering between the incident flux and ultra fine particles resulting from either aggregation from the vapor or blown off the liquid layer on the cavity wall is neglected. Energy losses due to Rayleigh scattering are inversely proportional to the fourth power of wavelength of the incident flux [18]. The Mie scattering can also be ignored because energy losses reduce with the sixth power of the size of particles [19].

(8) The effects of the refraction on the energy-beam are ignored. This is especially relevant for an Nd: YAG laser because the refractive index decreases with λ^2 [15].

Then, the distribution of the incident flux is proposed to be

$$q=\frac{3}{A_n}\exp\left[-3\left(\frac{\beta'}{\beta}\right)^2\right] \tag{1}$$

where constant 3 is chosen such that 95% of incident energy is included in solid angle β, the area of the spherical cap having the solid angle as the convergence angle yields

$$A_n=\int_0^{\beta}(2\pi s\sin\beta')s\,\mathrm{d}\beta'=2\pi s^2(1-\cos\beta). \tag{2}$$

In equation (2), the distance between the virtual or imaged point source and a point located at $z=z_i$ on the cavity wall is

$$s=\frac{1}{\cos\beta'}\left[\frac{r_f}{\tan\beta}+\mathrm{sign}(f+h)(f+h-z_i)\right] \tag{3}$$

where the function sign $(f+h)\equiv(f+h)/|f+h|=+1$ or -1 denotes the focal spot lying above or below the cavity base, respectively.

3. Monte Carlo method

The Monte Carlo method was used here to trace energy bundles and determine what fraction of the emitted energy has been absorbed and reflected by a surface or escaped from the system through an opening.

If N_i rays are imaged to leave $\mathrm{d}A_i$, all with energy ε_i/N_i where ε_i is the mean hemispherical emissivity of surface $\mathrm{d}A_i$, the sum of energies of the rays absorbed by surface $\mathrm{d}A_j$ will be the transfer factor, F_{ij}, and can be expressed as: [5]

$$F_{ij}=\varepsilon_i\lim_{N_i\to\infty}\left(\frac{N_{ij}}{N_i}\right) \tag{4}$$

where N_i and N_{ij} represent, respectively, the total number of energy bundles emitted by surface $\mathrm{d}A_i$, and the number of energy bundles emitted by surface $\mathrm{d}A_i$, which are eventually absorbed at surface $\mathrm{d}A_j$. For perfectly diffuse reflection, the fractional functions to determine the circumferential and cone angles of the emitted and reflected energy bundles yield, respectively:

$$P_\phi = \frac{\phi}{2\pi}, \quad P_\theta = \sin^2\theta \tag{5}$$

$$P_{\phi_r} = \frac{\phi_r}{2\pi}, \quad P_{\theta_r} = \sin^2\theta_r. \tag{6}$$

To determine if an energy bundle is absorbed or reflected, it is necessary to generate a random number. Provided that the random number is less than or equal to the absorptivity, the energy is completely absorbed. Otherwise, the remainder are all reflected.

If the position vector $\mathbf{R}_{ij}$ between the receiving point j and starting point i on the cavity is known, the specularly reflected ray $\mathbf{R}'_{ij}$ after striking point j can be described by the law of coplanarity and the law of reflection as:

$$\mathbf{R}'_{ij} = (\mathbf{n}_j \times \mathbf{R}_{ij}) \times \mathbf{n}_j - (\mathbf{n}_j \cdot \mathbf{R}_{ij})\mathbf{n}_j. \tag{7}$$

Hence, a trace of the specularly reflected component of the incident energy-beam would be accomplished.

The surface of the cavity is divided into N_r ring-elements. In view of the curvature of the cavity, each ring-element is further divided into N_e subdivisions. A random generator with a cycle $2^{31}-1$ generates photo numbers N_b. Convergence was tested by changing ring-elements, subdivisions and photo numbers. Choosing $N_r = 100$–200; $N_b = 1000$–2000; and $N_e = 20$, a relative deviation of energy flux absorbed was found to be less than 1% near the axisymmetric axis and 18% near the cavity opening where the incident flux is lowest. The deviation reduces to 10% near $r = 1$ by using subdivisions $N_e = 30$ and 40.

4. Analytical method

For the focal spot above the cavity base, an integral equation for radiant exchange in the cavity is given by

$$W(r_j) = \rho_d \left[q_j \cos(\psi_j - \beta'_j) + \int W(r_i)\, \mathrm{d}F_{(\mathrm{d}A_j - \mathrm{d}A_i)_t} + \sum_{n=1}^{\infty} \rho_s^n q_{jn} \cos(\psi_{jn} - \beta'_{jn}) \frac{\mathrm{d}A_{jn}}{\mathrm{d}A_j} \right] \tag{8}$$

where the first term on the right-hand side represents the radiation directly arriving at $\mathrm{d}A_j$ from outside the cavity through its opening, the second integral term gives the diffuse irradiation received by $\mathrm{d}A_j$ from all the elements on the cavity, the last summation term is the energy received by the element $\mathrm{d}A_j$ which has undergone only specular reflections on the surface before reaching $\mathrm{d}A_j$. In equation (8), the angle of an incident ray (see Fig. 1) impinging on a surface element at r_j is

$$\beta'_j = \tan^{-1}\left|\frac{r_j}{s_0 - hr_j^2}\right| \tag{9}$$

while inclination angle of a surface at r_j is

$$\psi_j = \tan^{-1}|2hr_j|. \tag{10}$$

The total view factor of the emitted radiation from $\mathrm{d}A_j$ that reaches $\mathrm{d}A_i$ by both direct and specular inter-reflections is [20]

$$\mathrm{d}F_{(\mathrm{d}A_j - \mathrm{d}A_i)_t} = \sum_{k=0}^{\infty} \rho_s^k f_k. \tag{11}$$

In equation (11), the fraction f_0 representing a diffuse view factor $\mathrm{d}F_{\mathrm{d}A_j - \mathrm{d}A_i}$ is derived to be

$$f_0 = \left\{ 1 - \frac{h^2(r_i^2 - r_j^2)^2[2(r_i^2 - r_j^2)^2 + 3(r_i^2 + r_j^2)h^2(r_i^2 - r_j^2)^2 + h^4(r_i^2 - r_j^2)^4]}{\sqrt{\{[(r_i - r_j)^2 + h^2(r_i^2 - r_j^2)^2]^3[(r_i + r_j)^2 + h^2(r_i^2 - r_j^2)^2]^3\}}} \right\} \cdot \frac{2r_i h^2}{\sqrt{1 + 4h^2 r_j^2}}\, \mathrm{d}r_i. \tag{12}$$

For the axisymmetric system, coordinates of three successive points are determined from the law of coplanarity and the law of reflection, which gives

$$r_{m+2} = \frac{4h^2 r_{m+1}^3 + 2r_{m+1} + r_m}{4h^2 r_m r_{m+1} - 1}, \quad m \geqslant 1. \tag{13}$$

Solving simultaneous equations (13) for $m = 1, 2, \ldots, n$, locations of points 1, 2, and $n+2$ are found to be related by

$$r_2 = R_n(r_1, r_{n+2}). \tag{14}$$

Replacing coordinate r_i in equation (12) by r_2 from equation (14), a relation between r_1, r_{n+2}, and r_j is obtained. Furthermore, r_1 and r_{n+2} are substituted by r_j and r_i, respectively. The fractions f_n of emitted radiation from $\mathrm{d}A_j$ striking $\mathrm{d}A_i$ after making n contacts with cavity surface yield [20]

$$f_n = \left\{ 1 - \frac{h^2(R_n^2 - r_j^2)^2[2(R_n^2 - r_j^2)^2 + 3(R_n^2 + r_j^2)h^2(R_n^2 - r_j^2)^2 + h^4(R_n^2 - r_j^2)^4]}{\sqrt{\{[(R_n - r_j)^2 + h^2(R_n^2 - r_j^2)^2]^3[(R_n + r_j)^2 + h^2(R_n^2 - r_j^2)^2]^3\}}} \right\} \cdot \frac{2R_n h^2}{\sqrt{1 + 4h^2 r_j^2}} \frac{\partial R_n}{\partial r_i}\, \mathrm{d}r_i \tag{15}$$

An incident ray striking a location (r_2, hr_2^2) from the source $(0, s_0)$ can be considered as an energy ray emitted from the location $(-r_1, hr_1^2)$ on the cavity wall along the straight line between these points. The relation between r_1 and r_2 yields

$$r_1 = \frac{s_0}{hr_2}. \tag{16}$$

Substituting equation (16) into equation (14), and replacing r_2 and r_{n+2} by r_{jn} and r_j, respectively, one can get

$$r_{jn} = R_n\left(\frac{s_0}{hr_{jn}}, r_j\right) \quad \text{or} \quad r_{jn} = U_n(r_j). \tag{17}$$

Once receiving point r_j is selected, the first impinging

point r_{jn} of incident ray arriving at r_j after n specular reflections, is determined by equation (17). The unknowns q_{jn}, ψ_{jn}, β'_{jn}, and dA_{jn}/dA_j can be evaluated.

4.1. Asymptotic solution

It is difficult to derive a general formulation of equation (8). For simplicity without loss of relevancy, equation (8) by taking $n = 1$ reduces to

$$W(r_j) = \rho_d\left[q_j\cos(\psi_j-\beta'_j)+\int W(r_i)(f_0+\rho_s f_1)\right.$$
$$\left.+\rho_s q_{j1}\cos(\psi_{j1}-\beta'_{j1})\frac{dA_{j1}}{dA_j}\right]. \quad (18)$$

In equation (18) the fraction is

$$f_1 = \left\{1-\frac{\begin{array}{r}h^2(R_1^2-r_j^2)^2[2(R_1^2-r_j^2)^2\\+3(R_1^2+r_j^2)h^2(R_1^2-r_j^2)^2+h^4(R_1^2-r_j^2)^4]\end{array}}{\begin{array}{r}\sqrt{\{[(R_1-r_j)^2+h^2(R_1^2-r_j^2)^2]^3[(R_1+r_j)^2}\\+h^2(R_1^2-r_j^2)^2]^3\}\end{array}}\right\}$$
$$\cdot\frac{2R_1h^2}{\sqrt{1+4h^2r_j^2}}\frac{\partial R}{\partial r_i}dr_i \quad (19)$$

where function R_1 obtained from equation (14) is

$$R_1(r_1,r_3) = \left[\frac{r_1+r_3}{8h^2}+\sqrt{\left(\frac{r_1+r_3}{8h^2}\right)^2+\left(\frac{1-2h^2r_1r_3}{6h^2}\right)^3}\right]^{1/3}$$
$$-\left[-\frac{r_1+r_3}{8h^2}+\sqrt{\left(\frac{r_1+r_3}{8h^2}\right)^2+\left(\frac{1-2h^2r_1r_3}{6h^2}\right)^3}\right]^{1/3}. \quad (20)$$

The quantities q_{j1}, β'_{j1}, ψ_{j1}, and dA_{j1}/dA_j on the right-hand side of equation (18), respectively, yield

$$q_{j1} = \frac{3}{A_n}\exp\left[-3\left(\frac{\beta'_{j1}}{\beta}\right)^2\right] \quad (21)$$

$$\beta'_{j1} = \tan^{-1}\left|\frac{r_{j1}}{s_0-hr_{j1}^2}\right| \quad (22)$$

$$\psi_{j1} = \tan^{-1}|2hr_{j1}| \quad (23)$$

$$\frac{dA_{j1}}{dA_j} = \frac{r_{j1}\sqrt{1+(2hr_{j1})^2}}{r_j\sqrt{1+(2hr_j)^2}}\frac{dr_{j1}}{dr_j} \quad (24)$$

where area A_n in equation(21) is determined from equations (2) and (3) by replacing z_j by z_{j1} corresponding to radius r_{j1}. From equation (17), we get

$$r_{j1} = U_1(r_j) = \frac{1}{2}\left\{\left[(-p+\sqrt{p^2-q^3})^{1/3}\right.\right.$$
$$\left.+(-p-\sqrt{p^2-q^3})^{1/3}-\frac{1}{3h^2}\right]^{1/2}$$
$$\pm\left[-(-p+\sqrt{p^2-q^3})^{1/3}-(-p-\sqrt{p^2-q^3})^{1/3}-\frac{2}{3h^2}\right.$$
$$\left.\left.-\frac{r_j(1-4hs_0)}{2h^2\sqrt{(-p+\sqrt{p^2-q^3})^{1/3}+(-p-\sqrt{p^2-q^3})^{1/3}-\frac{1}{3h^2}}}\right]^{1/2}\right\} \quad (25)$$

where

$$p \equiv \frac{s_0}{6h^5}+\frac{1}{432h^6}-\frac{r_j^2(1-4hs_0)^2}{32h^4} \quad (26)$$

$$q \equiv \frac{s_0}{3h^3}+\frac{1}{36h^4}. \quad (27)$$

Specular irradiation in equation (18) have two terms because of two roots of r_{j1} from equation (25). Two energy bundles therefore reach the receiving point r_j after one specular reflection.

4.2. Determination of distinct absorption regions

Energy absorption in the cavity is primarily determined by the first several specular reflections. Combing equation (16) with equation (13) in which m is taken to be 1, the first two striking points of an energy bundle are related by

$$r_3 = \frac{4h^2r_2^3+2r_2+\frac{s_0}{hr_2}\operatorname{sign}(f+h)}{4hs_0\operatorname{sign}(f+h)-1}. \quad (28)$$

A result of equation (28) is plotted in Fig. 3. For the

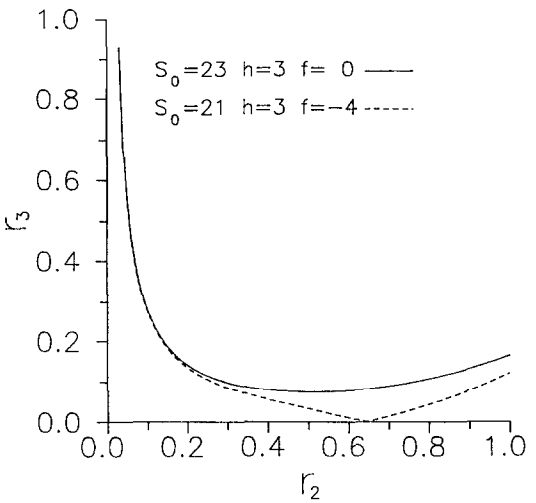

Fig. 3. Relation between locations of the first and second striking point of energy ray for the focal spot above and below the cavity base.

focal spot above the cavity base, an increase in the radius of the first striking point (r_2) from 0 to r'_S reduces the extrapolated radius of the second striking point (r_3) from infinity to unity. This indicates that the incident ray after the first specular reflection is escaped through the cavity opening to surroundings. A further increase in radius r_2 causes a rapid decrease in r_3. The minimum radius of the second striking point is found and defined as a dimensionless critical radius $r_3 = r_S$. The region $0 \leqslant r_3 < r_s$ does not experience incident rays after the first specular reflection. Therefore, the critical radius divides energy flux absorbed into two regions. Region I where $0 \leqslant r_3 < r_S$, experiences only the direct incident rays and diffuse irradiation. Aside from being exposed to the same irradiation as region I, region II where $r_S \leqslant r_3 \leqslant 1$ receive the second specular reflection from incident rays. The critical radius is obtained by setting $dr_3/dr_2 = 0$. This gives

$$r_s = \frac{2\sqrt{3}(12hs_0 - 1 + \sqrt{1+12hs_0})}{9h(\sqrt{1+12hs_0}-1)^{1/2}(4hs_0-1)} \tag{29}$$

which shows that the critical radius is only a function of the cavity depth and distance between the virtual point source and cavity base. Radii of the second striking point remain relatively constant near the critical radius for a wide range of r_2. Hence, most of the incident rays reach the neighborhood of the critical radius after the first specular reflection. Energy flux absorbed increases so abruptly that a jump occurs near the critical radius.

For a focal location below the cavity base, all locations $0 \leqslant r_3 \leqslant 1$ experience the second specular reflection. Only region II exists. The second striking points are mostly near the cavity base.

5. Results and discussion

In this work, energy absorbed by the cavity wall is governed by the dimensionless control parameters: the location (f) and the size (r_f) of the focal spot, the convergence angle (2β) of the energy-beam, depth (h), absorptivity (α), and specular reflectivity (ρ_s) of the cavity. Given a convergence angle and focal spot location, the focal spot size is chosen to satisfy relevant values of the dimensionless energy distribution parameter around 1–1.5 on the workpiece surface [3].

The variations in the critical radius with the location of the virtual point source for different cavity depths and convergence angles, as predicted by the Monte Carlo method and asymptotic solution from equation (29), are shown in Fig. 4. The computed results are confirmed by good agreement between two methods. Equation (29) can therefore be used to determine region I or II. Interestingly, the effect of convergence angle on the critical radius is insignificant. Decreasing rates of region I become small as the distance between the virtual point source and cavity base is greater than 10. The critical radius is then determined by the cavity depth.

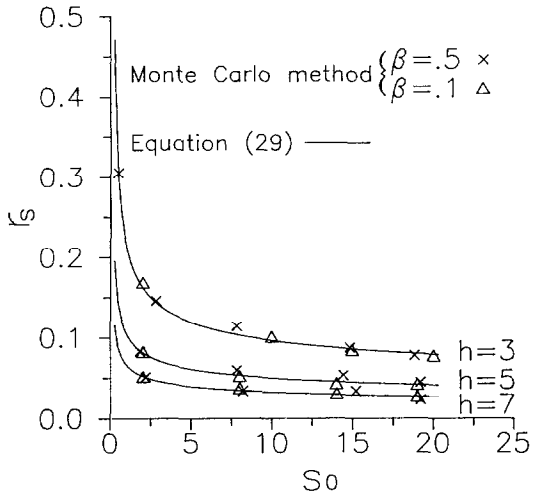

Fig. 4. Dimensionless critical radius vs distance between virtual point source and cavity base for different convergence angles and cavity depths, as predicted by Monte Carlo and asymptotic solutions.

Absorbed energy fluxes calculated by Monte Carlo method and asymptotic solution from equation (18) are also presented in Fig. 5. Typical values of dimensionless parameters are $f = 0$, $r_f = 1$, $\beta = 0.05$, $h = 3$, $\alpha = 0.5$, $\rho_s = 0.3$. It is seen that the asymptotic solution agree well with the Monte Carlo solution. The energy flux absorbed

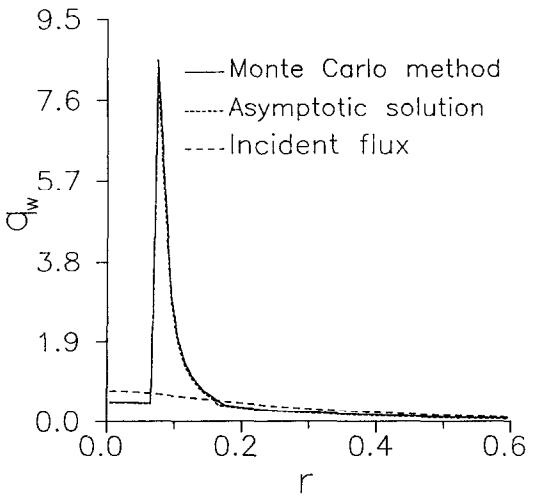

Fig. 5. Distribution of dimensionless absorbed energy per unit area of cavity wall by comparing Monte Carlo result with asymptotic solution from equation (18); incident flux is also shown ($f = 0$, $r_f = 1$, $\beta = 0.05$, $h = 3$, $\alpha = 0.5$, $\rho_S = 0.3$).

are apparently different from incident flux. A jump of absorption takes place in the case of a focused beam.

For focal spots above and below the cavity base, distributions of dimensionless energy absorbed per unit area of the wall for different spot sizes are shown in Fig. 6. Focal locations of −4 and 0 represent the focal spot below and above the cavity base ($h = 3$), respectively. In the case of focal location $f = 0$ energy flux absorbed jumps at $r = 0.08$ and 0.07, respectively, for different spot sizes. The location of the jump can be predicted from equation (29). On the other hand, the maximum energy flux absorbed occurs for the focal location $f = -4$ at the axisymmetric axis and several ten times higher than that induced by focal location $f = 0$. This is attributed to a great amount of specularly reflective rays arriving at the cavity base after the first specular reflection and a focusing effect of the image source. A decrease in the focal spot size enhances absorption in regions I and II. This is because incident flux with a small spot size is more concentrated than that with a large one when the beam is focused.

The variations of the focal spot location with energy flux absorbed are shown in Fig. 7. The focal locations are chosen to be 20, −2, −4 and −26. Focal locations of −4 and −26 represent focal spots below the cavity base, while −2 and 20 represent those above the cavity base. Focal locations are chosen such that distances of the focal spot from the cavity base are the same between −2 and −4, and 20 and −26, respectively. As the distance between the focal spot and cavity base decreases, energy flux absorbed increases in regions I and II. The critical radius indicating the location of the jump increases as the focal spot is descended toward the cavity

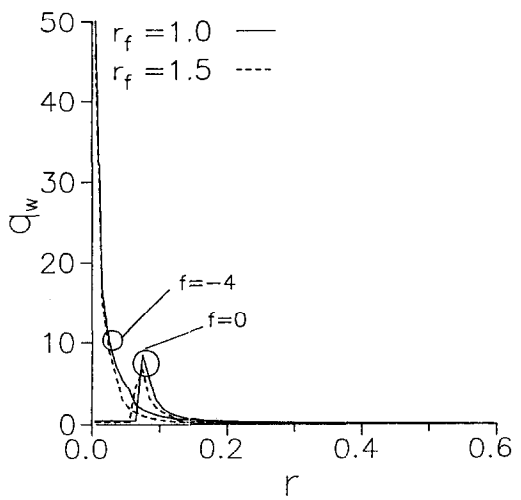

Fig. 6. Distribution of dimensionless absorbed energy per unit area of cavity wall for different spot sizes with focal locations above and below cavity base ($\beta = 0.05, h = 3, \alpha = 0.5, \rho_S = 0.3$).

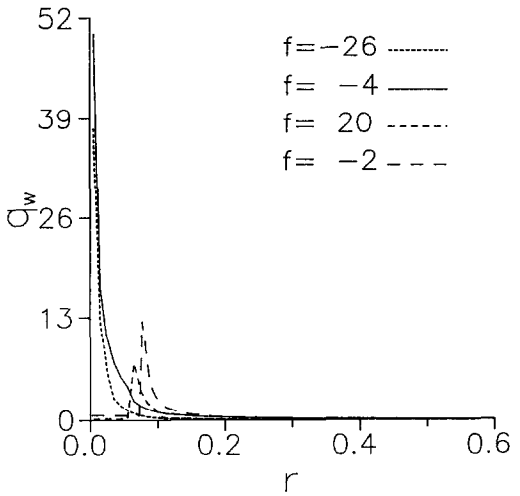

Fig. 7. Distribution of dimensionless absorbed energy per unit area of cavity wall for different focal locations ($r_f = 1, \beta = 0.05, h = 3, \alpha = 0.5, \rho_S = 0.3$).

base. For the focal spot below the cavity base, the jump disappears, while the maximum absorption occurs at the axisymmetric axis.

The fusion zone becomes V-shaped for the focal spot lying below the cavity base, as observed by Adams [1, 2], Konkol et al. [7], and Schiller et al. [10]. Spiking was associated with the V-shaped fusion zone as the focal spot was further lowered below the workpiece surface. The present work reveals that on slightly lowering the focal spot from above to below the cavity base, the absorbed flux readily increases by several hundred times near the axisymmetric axis. The cavity base therefore suffers strong melting. This leads to the cavity base lying below the focal spot again—and a subsequent decrease in energy absorbed and depth of cavity. The process is cyclically repeated. The free surface of the cavity base can also spontaneously oscillate. Hence, it is proposed that slight relative upward and downward oscillations between the focal spot and the free surface near the cavity base can be responsible for spiking.

Distributions of energy flux absorbed for different convergence angles are shown in Fig. 8. The energy beam becomes concentrated by reducing the convergence angle. As a result, a decrease in the convergence angle enhances energy absorption. The flux absorbed for the focal spot below the cavity base is still much higher than that above the base.

Distributions of energy flux absorbed by different cavity depths and focal locations are shown in Fig. 9. A deep cavity enhances absorption as a consequence of the increase in the amount of specular reflections and diffuse irradiation. Absorption varies more significantly with the focal spot being from below (above) to above (below) the cavity base for a deep cavity. Interestingly, two jumps

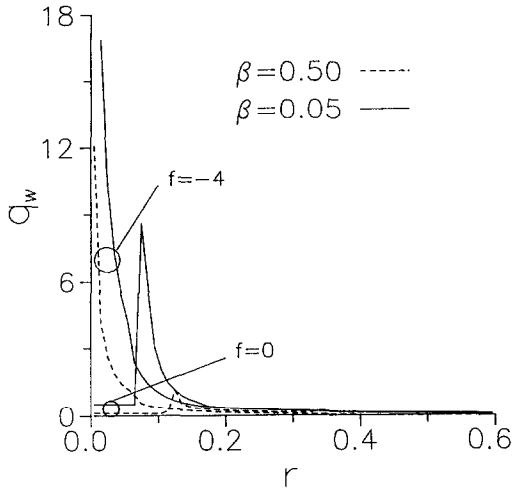

Fig. 8. Distribution of dimensionless absorbed energy per unit area of cavity wall for different convergence angles with focal locations above and below cavity base ($r_f = 1$, $h = 3$, $\alpha = 0.5$, $\rho_S = 0.3$).

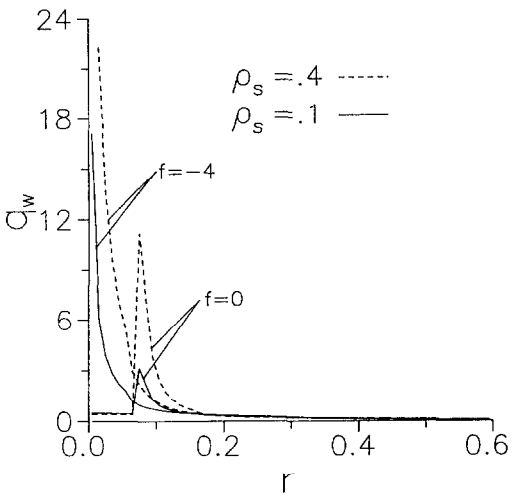

Fig. 10. Distribution of dimensionless absorbed energy per unit area of cavity wall for different specular reflectivities with focal locations above and below cavity base ($r_f = 1$, $\beta = 0.05$, $h = 3$, $\alpha = 0.5$).

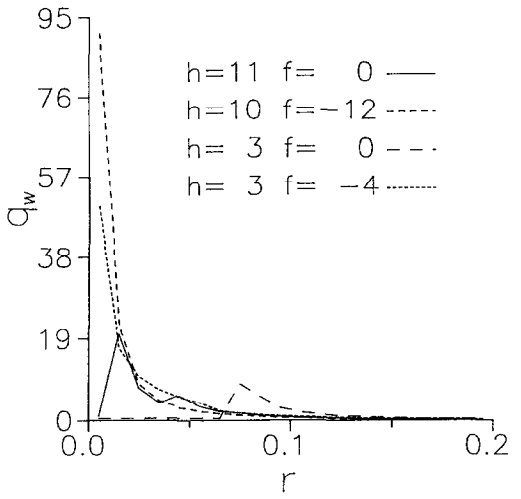

Fig. 9. Distribution of dimensionless absorbed energy per unit area of cavity wall for different focal locations and cavity depths ($r_f = 1$, $\beta = 0.05$, $\alpha = 0.5$, $\rho_S = 0.3$).

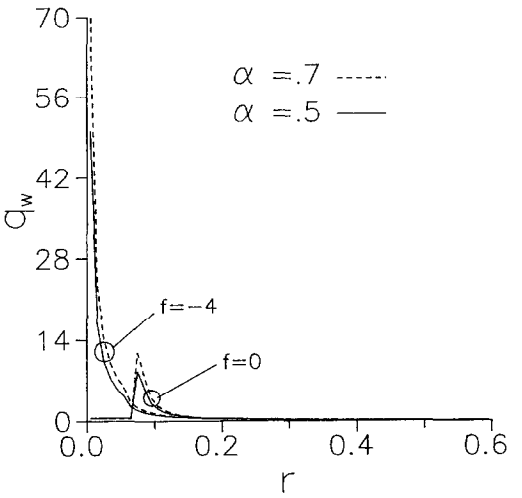

Fig. 11. Distribution of dimensionless absorbed energy per unit area of cavity wall for different absorptivities with focal locations above and below cavity base ($r_f = 1$, $\beta = 0.05$, $h = 3$, $\rho_S = 0.3$).

occur at a cavity depth $h = 11$. The second jump results from a third specular reflection. Therefore, energy absorbed is further increased. Irie et al. [11] proposed that the locally expanded fusion zone occurs near the middle of the depth. This defect may be a result of the jump due to the second or third specular reflections.

Figure 10 shows the effect of different specular reflectivities on energy flux absorbed. The extent of the jump is enhanced by increasing the specular reflectivity irrespective of focal locations above or below the cavity base. An increase in absorptivity increases energy absorption, as shown in Fig. 11. The maximum energy fluxes absorbed for absorptivity of 0.7 is approximately 1.4 times greater than that of 0.5.

The effects of the beam focusing characteristics on energy absorption are summarized in Table 1.

6. Conclusions

The Monte Carlo results are confirmed by asymptotic solutions. Conclusions can be drawn as follows:

Table 1
Effects of focusing parameters

	Parameter		Flux absorbed Reg. I	Flux absorbed Reg. II	r_S
$f > -h$	f	↑	↓	↓	↓
	β	↑	↓	↓	↑
	r_f	↑	↓	↓	↓
	h	↑	↑	↑	↓
$f < -h$	f	↓	None	↓	0
	β	↑	None	↓	0
	r_f	↑	None	↓	0
	h	↑	None	↑	0

(1) When the focal spot is above the cavity base, the energy flux absorbed by the cavity wall exhibits distinct regions. Region I, $0 \leqslant r < r_S$; and region II for $r_S \leqslant r \leqslant 1$. In region I, the energy absorbed is primarily the incident ray which after the first specular reflection escapes through the cavity opening to surroundings. In region II, energy absorbed additionally includes the second specular reflection. Any location in region II will be subject to the second strike from two different rays. As most of the second specularly reflected rays strike near the critical radius, absorbed energy exhibits a jump. A second jump can also occur for a deep and narrow cavity.

(2) When the focal spot is below the cavity base, region I disappears and absorption increases significantly. Absorption exhibits a sudden increase near the axisymmetric axis as the focal spot changes from above to below the cavity base. This variation is enhanced by increasing the cavity depth. Adjusting the focal spot below the cavity base is the most important way to increase energy absorption.

(3) The critical radius is a function of the cavity depth and distance between the virtual point source and cavity base. Influence of the convergence angle, however, is insignificant. For a large displacement of the point source from the cavity base, the critical radius remains relatively constant. The critical radius is therefore determined by the cavity depth.

(4) Energy absorbed is increased by reducing the distance between the focal spot and the cavity base, spot size, and convergence angle, and increasing the cavity depth, irrespective of the focal spot above or below the cavity base.

(5) The occurrence of spiking in welding is proposed to be relative upward and downward motions between the focal spot and cavity base. Since region I changes instantaneously from zero to maximum and vice versa, and the associated difference in energy flux absorbed by several hundred times, strong and periodic melting occurs at the cavity base. On the other hand, the abnormally expanded fusion zone at the middle portion of penetration can be a result of the first or second jump of energy flux absorbed.

(6) The effects of the beam focusing characteristics and radiative properties of the cavity wall on absorption are crucial for a relevant determination of energy transport to the workpieces. This work can also be applied for a design of solar collectors.

References

[1] Adams MJ. Low voltage electron beam welding: effect of process parameters. British Welding 1968;15:134–42.

[2] Adams MJ. High voltage electron beam welding-effect of process parameters. British Welding 1968;15:451–67.

[3] Wei PS, Chow YT. Beam focusing characteristics and alloying element effects on high-intensity electron beam welding. Metallurgical Transactions B 1992;23B:81–90.

[4] Arata Y. Plasma, Electron and Laser Beam Technology. American Society for Metals, Metals Park, Ohio, 1986, pp. 217–25.

[5] Toor JS, Viskanta R. A numerical experiment of radiant heat interchange by the Monte Carlo method. International J Heat and Mass Transfer 1968;11:883–97.

[6] Wang SC, Wei PS. Energy-beam redistribution and absorption in a drilling or welding cavity. Metallurgical Transactions B 1992;23B:505–11.

[7] Konkol PJ, Smith PM, Willebrand CF, Connor LP. Parameter study of electron-beam welding. Welding J 1971;50:765–76.

[8] Armstrong RE. Control of spiking in partial penetration electron beam welds. Welding J 1970;49:382(s)–8(s).

[9] Giedt WH. A Periodic melting model of high intensity electron beam welding. In: Rappaz M, Özgü MR, Mahin KW, editors. Modeling of Casting, Welding, and Advanced Solidification Processes—V, Davos. Switzerland: TMMMS, Warrendale, PA, Sep. 16–21, 1991. pp. 115–22.

[10] Schiller S, Heisig U, Panzer S. Electron Beam Technology. New York: Wiley, 1982. p. 317.

[11] Irie H, Tsukamoto S, Inagaki M. Relation between beam properties and shape of fusion zone in electron beam welding (Report I). J the Japan Welding Society 1982;51:941–5.

[12] Hicken GK, Giedt WH, Bentley AE. Correlation of joint penetration with electron beam current distribution. Welding J 1991;70:69(s)–75(s).

[13] Wei PS, Wu TH, Chow YT. Investigation of high-intensity beam characteristics on welding cavity shape and temperature distribution. ASME J Heat Transfer 1990;112:163–9.

[14] Miyazaki T. Material removal produced by a high-power-density electron beam. J Applied Physics 1977;48:3035–41.

[15] Poueyo-Verwaerde A, Fabbro R, Deshors G, de Frutos AM, Orza JM. Experimental study of laser-induced plasma in welding conditions with continuous CO_2 laser. J Applied Physics 1993;74:5773–80.

[16] Collur MM, DebRoy T. Emission spectroscopy of plasma during laser welding of AISI 201 stainless steel. Metallurgical Transactions B 1989;20B:277–86.

[17] Shui VH, Kivel B, Weyl GM. Effect of vapor plasma on the coupling of laser radiation with aluminum targets. J Quantitative Spectroscopy and Radiative Transfer 1978;20:627–36.

[18] Matsunawa A, Ohnawa T. Beam–plume interaction in laser materials processing. Transactions of Japan Welding Research Institute 1991;20:9–15.

[19] Duley WW. A comparison of keyhole absorption processes in laser and electron beam welding. Bakish R, editor. Proceedings of the Conference on the Laser vs the Electron Beam in Welding, Cutting, and Surface Treatment—State of the Art—1987. Englewood, NJ, U.S.A.: Bakish Materials Corp., 1987. pp. 160–7.

[20] Lin SH, Sparrow EM. Radiant interchange among curved specularly reflecting surfaces—application to cylindrical and conical cavities. ASME J Heat Transfer 1965;87:299–308.